Unprecedented Hemispheric Asymmetries During a Surprise Ionospheric Storm: A Game of Drivers

Elvira Astafyeva, Mala S Bagiya, Matthias Förster, Nozomu Nishitani

Unprecedented hemispheric asymmetries during a surprise ionospheric storm: a game of drivers

Elvira Astafyeva[1], Mala S. Bagiya[2], Matthias Förster[3,4], Nozomu Nishitani[5]

1 – Institut de Physique du Globe de Paris (IPGP), Université de Paris, 35-39 Rue Hélène Brion, 75013 Paris, e-mail: astafyeva@ipgp.fr;

2 – Indian Institute of Geomagnetism (IIG), Navi Mumbai, India;

3 – GFZ German Research Centre for Geosciences, Potsdam, Germany;

4 – Max Planck Institute for Solar System Research (MPS), Justus-von-Liebig-Weg 3, 37077 Göttingen, Germany*;*

5 – Institute for Space-Earth Environment Research, Nagoya University, Japan

Key Points:

- The 25-26 August 2018 storm caused several significant hemispheric asymmetries driven by very particular combination ("a game") of drivers

- In the ionosphere, strong opposite hemispheric asymmetries occurred during the main phase and during the recovery phases of the storm

- The asymmetry in the composition was unprecedented, the bulge went 20 degrees of latitude beyond the equator into the opposite hemisphere

Abstract

The geomagnetic storm occurred on 25-26 August 2018 as a surprise to forecasters. The arrival of a weak coronal mass ejection did not show a sudden impulse in the magnetic data, however, when the IMF Bz turned southward, it intensified and further remained unchangeably negative for the next 9 hours, causing a major storm with the minimum SYM-H excursion of –205 nT. In this work, we study the thermospheric, ionospheric and electrodynamic behavior during this storm. We use a set of space-borne (the Swarm constellation, GUVI/TIMED) and ground-based (GPS receivers, magnetometers, SuperDARN) instruments. We particularly focus on storm effects in the American and East Pacific sectors, where unprecedented hemispheric asymmetries occurred in the thermosphere and ionosphere during the main and the recovery phases of the storm. At the beginning of the storm, a strong positive ionospheric storm was observed in the Northern Hemisphere (NH), while in the Southern Hemisphere (SH), surprisingly, no storm effect occurred. During the recovery phase, the thermospheric composition ratio O/N_2 showed an extreme expansion of the bulge into the opposite hemisphere. Our analysis shows that in each case the asymmetry was produced by a unique combination of drivers that acted at particular moment of time and in particular place. The seasonal asymmetry in the high-latitude plasma and neutral mass density distributions along with the asymmetries in the geomagnetic field and the timing of these impacts played the decisive role.

Key words: geomagnetic storms, ionosphere, GPS TEC, prompt penetration electric fields, thermosphere, composition, electrodynamics, hemispheric asymmetry, Swarm, gradual commencement Sg storm

1. Introduction

Ionospheric response to geomagnetic storms, which is often referred to as an ionospheric storm, remains one of the most complex subjects in the solar wind-magnetosphere-ionosphere-thermosphere coupling system. The main challenge lies in the fact that the storm-time ionospheric behavior is controlled by several competing dynamic and electro-dynamic processes (drivers). Storm-time changes in the ionospheric plasma

density can be positive or negative with respect to the undisturbed values, and are traditionally referred to as “positive” and “negative” ionospheric storms, respectively.

A geomagnetic storm commences with the arrival of solar/interplanetary plasma at high velocity at Earth’s magnetopause. The most significant storms are caused by the plasma with southward-directed Bz component of the Interplanetary magnetic field (IMF). This sets up interconnection with Earth’s magnetic field lines and leads to a large amount of solar wind energy deposition into Earth’s magnetosphere [Gonzalez et al., 1994]. This phenomenon leads to a series of storm-time processes occurring throughout the globe that greatly modify the dynamics of the thermosphere and ionosphere.

At high-latitudes, particle precipitation, storm-driven enhanced ionospheric currents and rapid increase of the convection significantly alter the thermosphere- ionosphere system [e.g., Prölss, 1980; Fuller-Rowell, 2011]. The ionization and the plasma drift speeds at high-latitudes increase. The heated thermosphere expands and produces global changes in the thermospheric circulation. The storm-time winds blow from high to low latitudes. Joule and particle heating at high latitudes causes upwelling which enhance the molecular species in the upper thermosphere. This composition disturbance zone is further transported by the neutral winds to middle and low latitudes.

High-latitude convection electric fields penetrate into the low-latitude ionosphere (a phenomenon known as prompt penetration electric fields, PPEF) and play a significant role in the redistribution of the storm-time ionosphere. The PPEF have eastward polarity on the dayside and westward on the nightside [Huang et al., 2005; Kikuchi & Hashimoto, 2016; Bagiya et al., 2011; 2014]. On the dayside and in the post-sunset sector, the PPEF of eastward polarity reinforce the equatorial ionization anomaly (EIA) by producing plasma density enhancements in the EIA crests and plasma depletion over the magnetic equator. The position of the EIA crests can be shifted poleward from their undisturbed location by 5 to 15 degrees of latitude. These storm-time changes are known as the super-fountain effect [Tsurutani et al., 2004; Astafyeva, 2009; Astafyeva et al., 2007; 2015a; 2016a; Venkatesh et al., 2019], and by that provoke the overall enhancement of the low-latitude electron density. On the night-side, the PPEF of westward polarity cause downward plasma motion and a plasma depletion at low latitudes.

In addition to electric fields, the mid- and low-latitude ionosphere alter in response to storm-time changes in the thermosphere. The storm-driven neutral winds can raise or lower the F region electron density peak height, by pushing ions and electrons up or down along magnetic field lines, by that causing positive or negative ionospheric storms [e.g.,

Goncharenko et al., 2007; Lu et al., 2008; Paznukhov et al., 2009; Astafyeva et al., 2016b]. The disturbed thermospheric winds also drive meridional neutral winds that generate a westward/eastward electric field on the dayside/nightside, which opposes their quiet-time patterns [Blanc & Richmond, 1980]. Contrary to the PPEF that act almost immediately, the disturbance dynamo develops more slowly: it takes several hours to set up the disturbance winds and the associated dynamo electric fields, after which they can persist for many hours due to the neutral-air inertia (Maruyama et al., 2005).

Finally, storm-time changes in the thermospheric composition, a decrease/increase of the neutral density ratio O/N_2 may also lead to the occurrence of negative/positive ionospheric storms by increasing/decreasing the ion loss rate [e.g., Prölss, 1976; 1980; Fuller-Rowell et al., 1994; Crowley et al., 2006; Astafyeva et al., 2016a; 2018].

Therefore, the main drivers responsible for the storm-time ionosphere redistribution are more or less known. However, the ionospheric response to each storm is determined by a unique, complex, non-linear and even chaotic interaction of drivers playing their roles at a particular moment of time and in particular location. This presents major difficulty in the analysis of storm-time effects and, consequently, in forecasting the ionospheric behavior during geomagnetic storms even by using most comprehensive first-principles models [e.g., Borries et al., 2015; Huba et al., 2016; Astafyeva et al., 2017]. Therefore, further observations are important as they can help to better understand such a complex phenomenon as the ionospheric storm.

The main aim of this work is to study the ionospheric response to the 25-26 August 2018 geomagnetic storm in the American sector. We provide new observational evidence of a concurrent action of multiple drivers and their influence on the development of the ionospheric storm.

2. Data

In our study, we analyze the following observational data:

1) **Absolute vertical total electron content (VTEC**) as derived from ground-based GPS measurements. It is known that from dual-frequency GNSS measurements it is possible to calculate the VTEC from phase and code measurements and by removing the satellite and receiver biases [e.g., Rideout and Coster, 2006; Yasyukevich et al., 2016; Zakharenkova et al., 2016]. In this work, we use VTEC data with 5-min resolution

that are available from the Massachusetts Institute of Technology Haystack Observatory Madrigal database [Rideout and Coster, 2006]. To better understand the storm-time VTEC alterations (dVTEC), we remove 7-day averaged quiet-time reference values from the storm-time values. As the quiet-time reference, we took 7 least perturbed days in August-September 2018.

2) **Horizontal (H-) component of the geomagnetic field** as measured by ground-based magnetometers. From H- observations made by a pair of magnetometers, located one at the dip equator, and the other at ~6-9° of magnetic latitude away from it, we estimate the difference dH proportional to the equatorial electrojet (EEJ, e.g., Anderson et al., 2002; 2006; Yizengaw et al., 2012; 2014; Astafyeva et al., 2018). In this work, we use data from Jicamarca (76.8W; 11.9S) and Piura (80.6W; 5.2S) magnetic observatories that belong to the Low-Latitude Ionospheric Sensor Network (LISN).

3) **Cross-polar cap potential (Φ_{PC})** estimated from observations by the Super Dual Auroral Radar Network (SuperDARN). The SuperDARN is a global high-frequency (HF) radar network spread over the high and mid latitude regions to study the ionospheric variability over a large scale (Greenwald et al., 1995). The network consists of total 36 radars, 23 in the northern hemisphere and 13 in the southern hemisphere (Nishitani et al., 2019). The radars measure the line of sight plasma velocity which scrutinized further by fitting a model based on the spherical harmonic expansion to obtain the convection patterns over the high latitudes (Ruohoniemi and Baker, 1998). The derived ionospheric plasma convection maps provide initial measures of the electrodynamics at high latitudes, especially during geomagnetic storms. The typical convection map could be seen in Figure 6. It could be seen that the maps also contain the estimation of the cross-polar cap potential obtained from the voltage difference between the core of the dawn and dusk convection cells.

4) **In-situ electron density (Ne)** observations performed by the Langmuir Probe onboard Swarm A spacecraft at ~460km of altitude. The Ne is the Swarm Level 1b product. Swarm is a constellation of three identical satellites called A (Alpha), B (Bravo) and C (Charlie). Swarm A (SWA) and C are flying in a tandem at averaged orbital altitude of 460 km. While Swarm B (SWB) is placed at ~520km of altitude. During the August

2018 storm, SWA crossed the equator around 14.4 LT and 2.4LT, while SWB did it at ~21.6LT and ~9.6LT. In this work, we mostly analyze data from Swarm A (SWA).

5) **Vertical electron content (VEC**) above ~460km of altitude estimated from observations by the GPS-receiver onboard the Swarm satellite. Similar to the ground-based GPS-receivers, the VEC can be calculated from phase and code measurements, and by removing satellite and receiver bias [e.g., Zakharenkova & Astafyeva, 2015]. The VEC reflects the topside part of the VTEC.

6) **Thermospheric neutral mass density (ρ)** derived from the GPS-receivers onboard Swarm satellites. The thermospheric densities are calculated based on the estimation of accelerations, by separating non-gravitational forces acting on the spacecraft (aerodynamic drag) from other forces that can be accurately modelled [van den IJssel and Visser, 2007; van den IJssel, 2014; Astafyeva et al., 2017; March et al., 2019]. The neutral mass density is a Swarm Level-2 product. The variance for these data may reach 30% from models for neutral density [Swarm Data Handbook].

7) **Thermospheric O/N_2 composition** measured by the Global Ultraviolet Imager (GUVI) on board the Thermosphere, Ionosphere, Mesosphere Energetics and Dynamics (TIMED) satellite [Christensen et al., 2003]. The GUVI instrument measures a narrow swath below the satellite at 625 km altitude during the dayside spacecraft passages. Overall, the satellite provides 14.9 daily orbits. During the two days of the August 2018 storm, the time of the equatorial crossing was ~13.3-13.5 LT, i.e., about 1 hour ahead of SWA.

3. The surprise storm of 25-26 August 2018

A major geomagnetic storm occurred on 25-26 August 2018 as a surprise to forecasters. A minor coronal mass ejection (CME), associated with a small filament eruption on 20 August 2018, arrived at Earth on 25 August 2018 [Vanlommel, 2018]. The CME itself was too weak to be automatically detected by tools developed for that purpose. After additional manual analysis, the CME was estimated to have an Earth-directed component, however, its effects were expected to be minor. While the prediction that the

CME would impact Earth was correct, the strength of this slow moving interplanetary CME was quite a surprise.

The CME shock arrived at 2:45UT on 25 August 2018 [Blagoveshchensky and Sergeeva, 2019] but did not cause a sudden geomagnetic impulse (Figure 1a). The first shock was followed by the arrival of the CME material at ~7:45UT that compressed the magnetosphere and marked the beginning of the initial phase of the storm (Figure 1). From ~17UT, the IMF Bz turned southward and remained unchangeably negative for the next 10 hours, causing a strong geomagnetic storm.

Solar wind speed data show three small increases of ~50 km/s occurred during the day of 25 August 2018, the last one occurred ~3 hours before the storm began (Figure 1a). On 26 August, the speed was around 400 km/s during the first half of the day but from ~12UT it increased to the maximum of 566 km/s. The IMF Bz component was northward during the first half of the day on 25 August. From ~17UT, it turned southward and intensified down to –17 nT (Figure 1b). The IMF Bz remained largely negative until ~10UT of the next day, when it returned to zero level for a brief moment of time. Between ~10 and 21UT the IMF Bz showed several large-amplitude fluctuations. From ~10.1UT, the IMF Bz became negative again. This latter event lasted until ~13UT. The IMF Bz further was southward again from ~14.2UT to 18UT. The last small negative fluctuation was observed from 18.5 to 20.3UT.

The interplanetary electric field (IEF) east-west Ey component, that depends on the IMF Bz and on the solar wind speed as –Vsw * Bz (King and Papitashvili, 2005; https://omniweb.gsfc.nasa.gov/html/ow_data.html), did not show strong fluctuations during this storm (Figure 1c). The IEF Ey remained positive (eastward) during the main phase of the storm and reached the maximum of only 7.6 mV/m at 2-6UT on 26 August 2018.

The SYM-H index started to gradually descend from ~17.5UT (Figure 1d). From ~20 to ~22.5UT it remained at a “plateau” level of about –28-30 nT. From ~23UT, the SYM-H began to drop faster and reached the minimum of –207 nT at 5UT on 26 August. From ~7UT, the SYM-H index then continued to slowly grow up but remained below zero until 31 August 2018. From the point of view of the minimum SYM-H excursion, this storm has become the third strongest in the 24th solar cycle, just below the St. Patrick’s Day storm of 17-18 March 2015 and the 22-23 June 2015 event.

The storm of 25-26 August was accompanied by enhanced substorm activity. Variations of the auroral electrojet indices - AU (amplitude upper) and AL (amplitude lower) and the auroral electrojet (AE) – are shown in Figure 1 (f-g). It should be pointed out that

those are preliminary data from the World Data Center for Geomagnetism in Kyoto (WDC-Kyoto, http://wdc.kugi.kyoto-u.ac.jp/) and might contain some errors. Unfortunately, the provisional data sets are not yet available (Prof. S. Taguchi, private communication). The AU and AL indices characterize the maximum magnetic effects of the eastward and westward auroral electrojets, respectively. Figure 1(f) shows that both AU and AL started to grow from 16UT, and were symmetrically disturbed up to ±500nT until ~23 UT on 25 August. Starting from ~3.5UT on 26 August, the AU decreased down to ~50nT while the AL increased in intensity and showed fluctuations of -1500nT – 2000 nT. The maximum disturbance in the AL index was reached by 7.5-8.5 nT.

Such behavior of the AU and AL indices determined the behavior of the AE index, which represents the difference between the AU and AE indices. It started to grow gradually from 16UT on 25 August and arose up to 1000 nT by 19.3-23UT (Figure 1g). The maximum of ~2200 nT was reached at 7.5-8.5UT on 26 August 2018, i.e., at the beginning of the recovery phase of the storm.

4. Results

In this work, we focus on effects of the 25-26 August 2018 storm around the American and East Pacific region only (i.e., between -180 and -10 degrees of longitude). A detailed global overview is a subject of our future work.

4.1. Electrodynamic and Ionospheric effects. Ground-based observations

Figure 2 (a-c) shows electrodynamic and ionospheric behavior as observed by ground-based instruments. The longitude chosen for the VTEC analysis is 77W which is close to that of the magnetometers.

Before the storm commencement, the horizontal component of the magnetic field (dH) did not show any notable deviations from the quiet-time levels (Figure 2c). In the ionospheric VTEC, we observed only small changes at low-latitudes (Figures 2a and 2b).

At ~17UT, the IMF Bz turned southward and the storm began. However, the dH data did not exhibit significant enhancements typical of the dayside PPEF effects during major geomagnetic storms. Further, from ~18 to 22UT, the IMF Bz remained steadily southward, but the dH dropped slightly below the quiet-time level (Figures 2c and 2e).

In the ionosphere, no remarkable storm-time changes in the ionospheric VTEC were observed at the beginning the storm. In the SH, there occurred a small increase at low

latitudes similar to pre-storm conditions (Figure 2b). In the NH, small dVTEC started to occur with the storm onset at low (~15°N) and high-latitudes (~60°N) simultaneously (Figure 2b). These two ionization spots in the NH were, most likely, driven by different drivers: particle precipitation at high-latitudes, and the EIA at low latitudes.

Note that at this stage of the storm the VEC above Swarm A and B spacecrafts only showed small gradual increase (Figure 1e). Therefore, we conclude that the PPEF were rather weak at the beginning of the storm, which can be due to the unusual gradual beginning of this storm, and also due to the slow rate of change of the SYM/H with time at the beginning of the main phase of the storm.

From ~21UT, the VTEC response became highly asymmetric (Figures 2a and 2b). The enhancements in the NH continued to develop and moved towards one another to form one big spot of ionization (Figure 2b). From ~21:30UT, we observe significant enhancement at middle and low latitudes of the NH, and a small depletion of -2-4TECU at high-latitudes (~60°N). At mid-latitudes, the positive VTEC variations continued to intensify until ~1-2UT. At low latitudes, the storm-time dVTEC enhancement lasted until ~4-5UT and exceeded the quiet-time levels by +14+16TECU. By that time, the high-latitude depletion descended to 30°N (Figures 2a and 2b). The observed VTEC depletion had a latitudinal extent of about 8-10 degrees. It is, most likely, related to the storm-time expansion of the auroral oval (e.g., Afraimovich et al., 2004). It is interesting to note that we observed an enhancement of ~4-8TECU on the north from this VTEC depletion (Figure 2b).

From 2 to 4 UT one can see a dVTEC decrease at the magnetic equator and an increase at low latitudes in both hemispheres. These features are the signs of the development of the super-fountain effect, which often takes place at the evening LT hours [Kikuchi & Hashimoto, 2016; Astafyeva et al., 2015a;b].

From 7UT, the recovery phase began. During this period of time, the dH showed remarkable deviations from the quiet-time pattern (Figure 2c). At 11UT (6LT), the dH dropped by -20-40 nT instead of growing up, and by 13UT (8LT) it went above 0 nT. The dH turned again negative at 16UT(11LT), and then started to grow up from ~17.5UT and reached 50 nT by 20UT. It should be emphasized that these dH fluctuations only partly coincide with the variations of the IMF Bz (Figure 2e).

The ionospheric effects in the American region during the recovery phase are quite peculiar. The absolute VTEC shows only a moderate dayside maximum of ~20-22 TECU

within the equatorial region (Figure 2b). In terms of storm-to-quiet residuals, the ionospheric effects are very asymmetric. First, from 11UT (6LT), we notice a ~12-15TECU increase at low latitudes in both hemispheres and stronger ~18TECU increase at middle latitudes in the SH (Figures 2a,b), while above 50°N a depletion is observed.

Starting from ~16UT, a dVTEC depletion occurred at low and partly mid-latitudes of the NH. From 16 to 19.6UT the VTEC went by -10TECU below the quiet-time value, and the depletion was even stronger (-16TECU) from 21 to 24 UT on 26 August 2018. Whereas, in the SH signatures of positive ionospheric storm were observed (Figure 2c).

It should be noted that such storm-time changes and the VTEC pattern are similar throughout all American sector, from 180°W to 10°W (partly seen in Figures 3-5).

4.2. Ionospheric and thermospheric effects. Space-borne observations.

During the 25-26 August 2018 geomagnetic disturbance, Swarm A and GUVI/TIMED flew several times over the American Sector and brought additional evidence about the storm-time behavior of the thermosphere and ionosphere (Figures 3-5).

Figure 3 shows the beginning of the storm development, from ~18.5 to ~24UT on 25 August, i.e., starting from 1.5 hours after the IMF Bz turned negative. Note that these observations correspond to the daytime half-orbits. At 18.53-19.31UT (row A, Figure 3), both ionospheric parameters VEC (column SWA-V) and Ne (column SWA-N) showed a negative storm over low latitudes and no storm-time changes at other latitudes. Such behavior observed 1.5 hours after the storm onset could be an indication of the occurrence of the westward equatorial electric fields suppressing the EIA, an effect opposite to the super-fountain effect [e.g., Tsurutani et al., 2004; Astafyeva, 2009]. These observations are in line with the electrodynamic observations as discussed in Section 4.1.

During this period of time, the thermospheric neutral mass density (SWA-ρ) increased by 1-2 $*10^{-12}$ kg$*$m^{-3} throughout all latitudes, and reached the maximum of $3.2*10^{-12}$ kg$*$m^{-3} at mid-latitudes of the NH. Whereas, the thermospheric composition (column GUVI-O/N_2) did not change (Figure 3, row A).

Starting from ~20UT, the VEC and Ne started to increase at low-latitudes of the NH, and small positive storms (i.e., enhancements over the quiet-time levels) can be seen at middle latitudes (Figure 3, row B). Moreover, one can see the occurrence of ~5TECU positive storm in VEC at ~60-65°N. This can be a signature of a travelling ionospheric

disturbance (TIDs) of the auroral origin [e.g., Zakharenkova et al., 2016], that often occur during geomagnetic storms. Note that this enhancement is in line with ground-based VTEC results (GPS-VTEC column).

During this period of time, the thermospheric composition (ratio O/N_2) showed a small decrease with respect to quiet-time levels at high latitudes (~60°N) in the NH (Figure 3, row B). By this time, the thermospheric neutral mass density exhibits stronger storm-time changes than the O/N_2. The ρ in the NH exceeds the quiet-time level by ~1.5 times.

During the next daytime satellite passes, strong asymmetric effects were observed in both ionospheric and thermospheric data (Figure 3, row C). Both the VEC and Ne largely increased at low latitudes and at middle and high latitudes in the NH. These space-borne observations are in line with ground-based VTEC results.

In the thermospheric neutral mass density, we observe much stronger effects in the NH, especially at mid-latitudes where the ρ reaches $6*10^{-12}$ $kg*m^{-3}$, which is more than 100% more than during the undisturbed time. In the SH, storm-time alterations at mid- and high-latitudes are much less pronounced. The composition ratio O/N_2 shows small deviations at high latitudes, and the effect is stronger in the SH.

Similar effects were observed during the next overflies of the satellites over the American region (Figure 3, row D). In both VEC and Ne data, we see the signatures of TIDs at 60°S. Also, the neutral mass density increased in the SH with respect to the previous observations.

The next passage of the SWA satellite over the American sector took place between ~4.6 and ~10.10UT on 26 August (Figure 4). This period of time corresponds to the end of the main phase and beginning of the recovery phase. Note that these observations were performed during local night hours (~2.4LT), and GUVI data were not available since the instrument only performs the measurements on the dayside. The night-time ionospheric observations by SWA showed signatures of a negative ionospheric storm (columns SWA-V and SWA-N).

It is interesting to note that during this period of time the ground-based VTEC showed the occurrence of the extremely large-scale VTEC enhancements occurring around 50°N along the whole territory of the USA (Figure 4, column 1, GPS-VTEC). This feature can, most likely, be interpreted as the large-scale TIDs [e.g., Pradipta et al., 2016; Zakharenkova et al., 2016]. These TIDs, however, were not observed in the space-borne

data, indicating that they occurred in the lower ionosphere, at least below the SWA altitude, i.e., below 460 km.

Contrary to the space-borne ionospheric observations, the thermospheric night-time storm signatures were quite significant (column SWA-ρ, Figure 4). The storm-time features are similar during all four passes. As on the dayside, the observed night side ρ increase is hemispherically asymmetric with stronger effects in the NH. This is related to the seasonal effect, when northern polar region is sunlit during most of the time, which leads to higher neutral concentration even for the quiet-time thermosphere (thin lines). This seasonal effect was superposed by the storm-time thermospheric response.

Note that the absolute values of the storm-time deviations increase in amplitude quite rapidly with time. Thus, during the first flyover, the SWA-ρ reached 1.5-2*10^{-12} kg*m^{-3} in the SH, which is ~150-200% more than during the quiet time (row A). In the NH, the neutral mass density increased up to 4 *10^{-12} kg*m^{-3} at low latitudes and up to 5-6.5 *10^{-12} kg*m^{-3} at middle and high-latitudes. These enhancements represent ~300-400% of the undisturbed value (shown by thin curves). Further, the thermospheric neutral mass density continued to increase, and, by 9.3-10.10UT the storm-time effect reached 300% at high latitudes in the SH, 500% at low latitudes and up to 600% at high latitudes in the NH (Figure 4, row D, rightmost column of panels).

The next passages of the SWA and GUVI satellites over the American region occurred between ~16.3 and ~21.7 UT on 26 August. This period of time corresponds to the recovery phase of the storm, i.e. more than 23 hours after the storm onset, and 9 hours after the beginning of the recovery phase. The topside VEC and the in-situ observations by SWA are presented in Figure 5, columns 2 (SWA-V) and 3 (SWA-N), respectively. As often observed during the recovery phase, the VTEC and Ne decreased as compared to the main phase, i.e. we observe negative ionospheric storm. During the first two flyovers, from 16.3UT to ~18.65UT (Figure 5, rows A and B), the storm-time Ne at high and middle latitudes does not exceed the background values, while the low-latitude Ne changed quite drastically. The position of the Ne peak shifted southward, but the amplitude of the peak's maximum remains around 3*10^5 m^{-3}, i.e. at the same level as during the quiet time. By the end of the day (19.4 – 22UT) the maximum electron density dropped below the quiet time values (Figure 5, rows C and D). This effect is more significant in the NH.

The behavior of the topside VEC is more complex (Column 2, Figure 5). At ~16.3-17.1UT, the maximum low-latitude VEC does not exceed 11 TECU and was shifted southward by 20-30 degrees of latitudes. The position of this storm-time increase coincides with the position of the dVTEC enhancement (Column 1). During the next SWA passage, the VEC shows a negative deviation from the reference level. By ~21UT, both the VEC and Ne experience negative deviation at low and mid-latitudes.

The observed southward displacement of the maximum VEC and Ne is due to the thermospheric impact, the oscillations (i.e., increase and decrease) of the equatorial and low-latitude VEC, most likely, occur in response to the IMF Bz positive-negative oscillations (Figure 1).

The thermospheric alterations during the recovery phase, in both the neutral density and the composition, were quite significant. The disturbance in the thermospheric neutral mass density reached ~8-10*10^{-12} kg*10^{-3} at middle and low latitudes, which is 300-500% increase as compared to the quiet-time level (Figure 5, 4th column, rows A and B). At high latitudes, the storm-time changes are smaller and reach 4.5-6*10^{-12} kg*10^{-3}, which represents 200-300% storm-time enhancement. The storm-time changes are asymmetric, with stronger effects in the NH. From ~19.43UT the ρ started to gradually decrease, but came back to undisturbed values only several days later (not shown here).

The storm-time effects in the thermospheric composition during the recovery phase of the August 2018 storm are unprecedented (Figure 5, the rightmost column). Thus, at ~16.15-16.89UT, significant depletion in the O/N_2 ratio occurred at high, middle and partly at low latitudes in the NH, as well as below ~ 50°S in the SH. Whereas, at latitudes between ~5°N and ~60°S the composition largely exceeded the reference level (Figure 5, row A). The O/N_2 showed similar asymmetric behavior during the next three flyovers by the TIMED spacecraft (rows B, C and D). It should be noted that the occurrence of the composition disturbance at high latitudes and its equatorward propagation due to the disturbed thermospheric winds is a commonly observed storm-time feature [e.g., Fuller-Rowell et al., 1994]. However, the hemispheric asymmetry in O/N2 observed during the August 2018 storm is unprecedented, since the depletion descended beyond the equator and reached ~15-20°S (Figures 5). Analysis of the O/N_2 ratio data for the whole period of observations by the TIMED satellite mission since 2002 (data are available here: http://guvitimed.jhuapl.edu/guvi-galleryl3on2) showed that the depletion rarely went beyond the equator.

Interestingly, even the solstice day storm of 22-23 June 2015, when the asymmetry was supposed to be much more pronounced due to the maximum seasonal impact, showed less asymmetric response [Astafyeva et al., 2016a].

5. Discussion

As demonstrated above, the 25-26 August geomagnetic storm produced several strong hemispherically asymmetric effects in the thermosphere and ionosphere over the American-Pacific region.

The observed storm-time variations of the thermospheric neutral mass density are rather “classic”, and are in line with previous observations [e.g, Liu and Lühr, 2005; Liu et al., 2005; Balan et al., 2011; Bagiya et al., 2014; Astafyeva et al., 2015a; 2017]. Both day and night side observations by Swarm A satellite showed stronger storm-time increment of the neutral mass density in the NH (summer), that can be attributed to seasonal effects [Fuller-Rowell et al., 1996]. The storm occurred two months after the June solstice and one month before the September equinox, i.e., the northern polar and auroral regions still received more solar energy than the southern ones. The quiet-time (background) thermospheric circulation is driven by the solar heating. In the NH (summer) it is directed equatorward, while in the SH (winter) hemisphere it is poleward. With the beginning of the main phase of the storm, the high-latitude heating drives global wind surges from both polar regions toward the equator. The (horizontal) neutral wind at all thermospheric altitudes strengthen tremendously due to an increased ion-neutral drag within the highly intensified and vastly extended convection cells in the polar region. On the dayside, in the summer hemisphere the storm-driven daytime circulation superposes to the background one, leading to easier transport of the high-latitude atmospheric disturbance to the opposite hemisphere. Meanwhile, in the winter hemisphere the storm-time circulation opposes the background circulation, and hampers the propagation of the high-latitude perturbations towards low latitudes. The night-side thermospheric circulation is also affected by the seasonal effects producing higher concentration in the summer hemisphere and a further increased efficiency of the ion drag forcing, which was the case during the August 2018 storm.

The storm-time changes in the neutral wind system could partly explain the observed alterations in the thermospheric composition. The compositional disturbance (also known as “composition bulge”) is initially generated at high latitudes due to the

energy injection at the storm onset. This composition disturbance is further transported by the global thermospheric winds out of the heated auroral area [Prölss, 1980]. However, as stated above, the asymmetry that occurred in the American & East Pacific region was unprecedented, as the depletion travelled ~20 degrees of latitude beyond the equator into the opposite hemisphere. Therefore, we conclude that very particular conditions developed in the course of the storm's main phase in the polar region of the NH in this longitudinal sector.

It is known that the magnitude of the compositional disturbance and its extension to lower latitudes are determined by the distribution and strength of the primary energy and momentum source (i.e., particle precipitation, Joule heating, ion-neutral drag), as well as by the dynamical response of the upper atmosphere itself, that in turn depends on the UT start of the storm. The energy injection is controlled by the geomagnetic field, so that the basic latitudinal variation in a geographic coordinate system should be that produced by the varying displacement between magnetic and geographic latitude [Prölss, 1976]. Consequently, the composition changes should be the strongest in the North American and in the Australian sectors where the magnetic latitude is the most displaced toward the equator. Indeed, these regions are often the most perturbed in terms of the storm-time composition alterations.

In terms of the UT dependence, the expansion of the polar atmospheric disturbance toward middle latitudes is essentially restricted to the midnight/early morning hours [Prölss, 1976; 1980; Fuller-Rowell et al., 1996]. It is known that the energy injection maximizes along the auroral oval, which is not symmetric in local time but is displaced toward the dark hemisphere [Prölss, 1980]. In addition to these driving forces, the enhanced substorm activity could strengthen the development of the composition storm effects [Prölss, 1976]. In the case of the August 2018 storm, the strongest asymmetry in the composition was observed around 100-70°W (Figure 5), which is, indeed, close to the longitude of the north geomagnetic pole. However, the main phase began at 17UT, i.e. when the American-Pacific region was already on the dayside (11-13LT). The main phase was preceded by weak substorm activity starting from ~16UT (Figure 1), however, we consider these pre-storm changes to be too insignificant to impact the storm development.

Analysis of the AU/AL indices variations (Figure 1) shows that the AL index increased remarkably during the second half of the main phase. Thus, at ~04:30-06:30 UT on 26 August they reached ~1500 nT. Moreover, even stronger growth down to -2000 nT was observed at the beginning of the recovery phase at ~07:30-08:30 UT. It should be

noted that during this period of time, the American region was in the early morning hours, i.e., the region of the strongest impact on the composition expansion toward low latitudes. Therefore, we consider that a combination of the factors of American region being along the longitude of the largest offset between the geographic and magnetic poles, and the strong auroral impact during the local early morning hours is responsible for producing the unprecedented hemispheric asymmetry in the thermospheric composition ratio O/N_2 observed during the recovery phase.

The ionospheric behavior during the August 2018 storm in the American/Pacific sector showed hemispheric asymmetry as well. During the main phase of the storm, a strong positive ionospheric storm was observed in the NH (summer), while no storm-time deviation occurred in the SH (winter). During the recovery phase, the NH experienced a strong negative storm, while in the SH only positive storm signatures were observed. It should be noted that both of these asymmetries are of the magnitude stronger than the average statistical storm-time asymmetrical effects.

The striking hemispheric asymmetry during the main phase is very unusual and is difficult to explain. As in the case of the composition changes, a very specific combination of drivers should have acted to produce such an asymmetry.

In the NH, the huge storm-time VTEC increase at middle and low latitudes seemed to be driven by a combination of the forcing from high (ionization and thermospheric winds) and low-latitudes (electric fields). From Figure 3 it follows that during this period of time, the thermospheric neutral mass density was higher in the NH than in the SH. Also, the Ne and VEC in the NH were more perturbed. These perturbations are indications of the stronger forcing coming from the North polar region in terms of high-latitude ionization and increased storm-time neutral winds.

In the SH (winter), very weak storm-time changes were observed in the ionospheric parameters, even at low latitudes. This is a very rare and the most puzzling observation, as quite often we observe positive storms in the winter hemisphere, or at least the response at low latitudes is asymmetric.

One of possible explanations is a combination of weak thermospheric winds in the SH and poor ionization in the SH because of the seasonal features. As known, the meridional equatorward thermospheric winds can produce positive ionospheric storms at middle and low latitudes by dragging the ions upward along the magnetic field lines. However, if the ionization is poor at high latitudes, then there is nothing to be transported by the winds (e.g., Astafyeva et al., 2016b).

525 The variations of the thermospheric neutral mass density during the beginning of the
526 main phase show weak perturbation coming from the polar regions in the SH, which is an
527 indication of weak equatorward winds coming from the SH polar region.
528 The hemispheric asymmetry in the high-latitude could come from several
529 phenomena as discussed before. In addition, the natural North-South asymmetries in the
530 geomagnetic field introduce differences in the magnetosphere–ionosphere–thermosphere
531 coupling in the two hemispheres [Laundal et al., 2017]. Indeed, there are significant
532 differences between the Earth's magnetic field in the Northern and Southern polar regions.
533 In addition, the longitudinal variation in magnetic flux density and field inclination are much
534 larger in the SH. Statistical studies showed that these asymmetries between the
535 hemispheres, both in strength and in orientation, lead to differences in the high-latitude
536 upper atmosphere in ionospheric plasma convection, magnetic field perturbations and
537 associated currents, thermospheric winds, plasma drifts and ion-neutral momentum
538 transfer [Tulunay and Grebowsky, 1987; Förster et al., 2011; Förster and Cnossen, 2013;
539 Coxon et al., 2016; Laundal et al., 2017].
540 To check possible difference between the NH and SH polar regions, we analyzed
541 variations of the cross-polar cap potential (Φ_{PC}), which is a good measure of the intensity
542 of the high-latitude electric field. The cross-polar cap potentials in the NH and SH as
543 estimated from SuperDARN observations during 25-26 August 2018 are shown in Figure
544 2f. One can see that before 15UT on 25 August, the Φ_{PC} in both hemispheres varied
545 between 26 and 32 kV. From 15UT, when the IMF Bz began to drop, the Φ_{PC} started to
546 grow but showed similar intensity variations (Figure 2f). At ~21UT on 25 August we
547 observe significant difference between the two hemispheres. In the SH, the Φ_{PC} dropped
548 to 55 kV, while in the NH it exceeded 90 kV. The asymmetry continued until ~3.5 UT on 26
549 August. We note that this period of time corresponds to the time when the strong
550 hemispheric asymmetry in the VTEC was observed in the American region (Figure 2b).
551 However, it should be pointed out that the Φ_{PC} value is largely impacted by the
552 SuperDARN radar coverage and by the latitudinal radar distribution (Nishitani et al., 2019).
553 For instance, Baker et al (2007) showed that the Φ_{PC} can increase because of more radars
554 operating at mid-latitudes in the NH. Figure 6 shows several examples of the ionospheric
555 convection patterns determined from SuperDARN radar observations during the period of
556 the significant South-North asymmetry in the VTEC, i.e. 21UT on 25 August to 3UT on 26
557 August. One can see that during this period of time, indeed, the convection zone in the NH

extended beyond 50°N. Such an extension undoubtedly had an effect on the large-scale convection pattern, including the resulting cross-polar cap potential between the two main cells.

In addition to the above mentioned seasonal effect, local time dependence and the geomagnetic field asymmetry, the IMF By (east-west) can be responsible for the development of the hemispheric asymmetry [e.g., Lu et al., 1994; Crowley et al., 2010; Pettigrew et al., 2010; Förster et al., 2011; Förster and Cnossen, 2013; Mannucci et al., 2014; Förster and Haaland, 2015; Laundal et al., 2017]. The IMF By modifies the ionospheric convection pattern and leads to a hemispheric asymmetry in the Region 1 (the poleward region) field-aligned currents (FACs). When the IMF By component is positive, the upward FACs on the dusk side of the SH are stronger. Under these conditions, the cross-polar neutral wind flow is on average stronger in the SH as compared to the NH under negative IMF Bz and positive IMF By conditions [Förster et al., 2011].

Variations of the IMF By component during the two days of the August 2018 storm are presented in Figure 2e. At the beginning of the main phase of the storm, the IMF By was largely negative (westward). Between ~22.5UT and 4UT the IMF By fluctuated around 0 nT and changed the polarity several times. From ~4UT on 26 August, the IMF By turned positive (eastward) and reached +18nT by 9UT. It further remained positive until ~20UT. The IMF Bz was positive through the entire main phase (Figure 2d). We conclude that the IMF By hardly played a role in the observed asymmetry during the August 2018 storm.

Finally, the ionospheric distribution during the recovery phase was, most likely, driven by the background seasonal effect in combination with the storm-time changes in the thermospheric composition. It is known that the composition has a drastic impact on the ionization [Prölss, 1980; Fuller-Rowell et al., 1994]. An increase in the molecular species causes an increase in the ionization loss rate, and a decrease of atomic oxygen causes a decrease of the ionization production rate; both these phenomena lead to the ionization decrease.

6. Summary

The geomagnetic storm of 25-26 August 2018 was a very particular event. The storm occurred as a surprise to forecasters. A weak CME was launched from the Sun on 20 August, and was too weak to be detected automatically in coronographic images. The CME arrived at Earth on 25 August 2018, and caused a major gradually commenced (Sg)

geomagnetic storm. However, while generally Sg storms are known as less intensive, the August 2018 storm has become the third strongest storm in the 24th solar cycle (minimum SYM-H of -205 nT), just below the 2015 St. Patrick's Day storm and the 22-23 June 2015 storm.

The August 2018 storm produced several unusual and strong effects in the electrodynamics, ionosphere and thermosphere that became apparent in particular in the American-to-East Pacific region:

1) During the first 2 hours of the main phase of the storm, the dayside PPEF were weaker as compared to other storms of similar intensity. This is, most likely, because of the gradual commencement of the storm. In addition, the enhanced substorm activity that preceded the main phase of the storm could have played a role;

2) In the thermospheric neutral mass density, the storm produced 300-500% increase with respect to the quiet-time values. The storm-time effects were stronger in the NH (summer);

3) In the thermospheric composition, a hemispheric asymmetry of unprecedented magnitude was observed during the recovery phase of the storm. This asymmetry could be explained by a very particular combination of drivers. Most likely, the seasonal asymmetry in the high-latitude plasma and neutral mass density distributions along with the asymmetries in the geomagnetic field have played the decisive role. The different offsets of the invariant poles (by a factor of two) at the NH and SH, together with important differences in the magnetic field strength within the polar caps of the NH and SH at ionospheric heights lead to a preference of the NH in favor of larger ion drift velocities and, hence, the ion drag forcing of the upper atmosphere (at least in the American-Pacific sector).

4) In the ionosphere over the American and East Pacific region, during the main phase, a strong positive ionospheric storm was observed in the NH (summer), while very weak storm-time effects occurred in the SH (winter). This is very unusual effect which occurred in the considered region due to the particular timing situation of this storm's development with respect to the longitudinal range of the main storm drivers.

5) During the recovery phase, a strong negative ionospheric storm occurred in the NH (summer) and a positive storm in the SH (winter). These changes are in line with previous observations and can be explained by the seasonal impact amplified by the storm-time alterations in the thermospheric composition.

Our study demonstrates, yet again, how chaotic and unpredictable can be the evolution of an ionospheric storm, and how a very peculiar combination of drivers can lead to extraordinary effects in the thermosphere and ionosphere.

Acknowledgment

We acknowledge the NASA/GSFC's Space Physics Data Facility's OMNIWeb service for the data of the interplanetary and geophysical parameters, and the World Data Center for Geomagnetism in Kyoto (WDC-Kyoto, http://wdc.kugi.kyoto-u.ac.jp/) for the data of the AU/AL and AE/AO indices. We are grateful to the OpenMadrigal web-service (http://cedar.openmadrigal.org) for the VTEC data used in this work. Data from ground-based magnetometer stations Jicamarca and Puira are available from http://lisn.igp.gob.pe. Low-Latitude Ionospheric Sensor Network (LISN) is a project led by the University of Texas at Dallas in collaboration with the Geophysical Institute of Peru and other institutions that provide information for the benefit of the scientific community. We thank the European Space Agency (ESA) for the Swarm mission data, that can be obtained from the ESA's EarthNet web services (http://earth.esa.int/swarm). We acknowledge the use of SuperDARN Data (http://vt.superdarn.org). SuperDARN is a collection of radars funded by national scientific funding agencies of Australia, Canada, China, France, Japan, South Africa, the United Kingdom, and the United States**.** The GUVI data used in this work are provided through support from the NASA MO&DA program and are available at: http://guvitimed.jhuapl.edu/data_products. The GUVI instrument was designed and built by The Aerospace Corporation and The Johns Hopkins University. The Principal Investigator is Dr. Andrew B. Christensen and the Chief Scientist and co-PI is Dr. Larry J. Paxton. This work was supported by the French Space Agency (CNES) and by Department of Science and Technology (DST), India. M.S.B. duly acknowledges the Institut de Physique du Globe de Paris, Paris for awarding the visiting scientist fellowship. MF and NN thank the 2019 ISEE International Research Program (Project "Relation of Swarm satellite and SuperDARN ground-based ion drift measurements". Figures 1-5 are

plotted by using the Generic Mapping Tools (GMT) software (Wessel and Smith, 1998). This is IPGP contribution 4100.

References

Afraimovich, E.L., Astafieva E.I., Berngardt O.I., Lesyuta O.S., Demyanov V.V., Kondakova T.N., and Shpynev B.G. (2004) Mid-latitude amplitude scintillation of GPS signals and GPS performance slips at the auroral oval boundary. *Radiophysics and Quantum Electronics*, v.47, N7, 453-468

Anderson, D., A. Anghel, K. Yumoto, M. Ishitsuka, and E. Kudeki (2002), Estimating daytime vertical ExB drift velocities in the equatorial F-region using ground-based magnetometer observations, *Geophys. Res. Lett*, 29 (12), 1596, doi: 10.1029/2001GL014562.

Anderson, D., A. Anghel, J.L. Chau, and K. Yumoto. (2006) Global, low-latitude, vertical ExB drift velocities inferred from daytime magnetometer observations, *Space Weather*, 4, S08003, doi: 10.1029/2005SW000193.

Astafyeva, E., E.L. Afraimovich, E.A. Kosogorov (2007) Dynamics of total electron content distribution during strong geomagnetic storms, *Advances in Space Research*, V.39, 1313-1317, doi:10.1016/j.asr.2007.03.006.

Astafyeva, E.I. (2009) Dayside ionospheric uplift during strong geomagnetic storms as detected by the CHAMP, SAC-C, TOPEX and Jason-1 satellites. *Advances in Space Research*, 43, 1749-1756, doi:10.1016/j.asr.2008.09.036.

Astafyeva, E., I. Zakharenkova, and E. Doornbos (2015a), Opposite hemispheric asymmetries during the ionospheric storm of 29–31 August 2004, *J. Geophys. Res. Space Physics*, 120, 697–714, doi:10.1002/2014JA020710.

Astafyeva, E., I. Zakharenkova, and M. Foerster. (2015b) Ionospheric response to the 2015 St. Patrick's Day storm: a global multi-instrumental overview. *J. Geophys. Res. Space Physics*, V.120, N10, 9023-9037, doi:10.1002/2015JA021629.

Astafyeva, E., I. Zakharenkova and P. Alken. (2016a) Prompt penetration electric fields and the extreme topside ionospheric response to the 22-23 June 2015 geomagnetic storm as seen by the Swarm constellation. *Earth Planets and Space,* V.68, doi:10.1186/s40623-016-0526-x.

692 Astafyeva, E., I. Zakharenkova, and Y. Pineau. (2016b) Occurrence of the dayside three-
693 peak density structure in the F2- and the topside ionosphere. *J. Geophys. Res.-*
694 *Space Physics,* V.121, N7, 6936-6949, doi:10.1002/2016JA022641
695 Astafyeva, E., I. Zakharenkova, J.D. Huba, E. Doornbos, J. van den IJssel. (2017) Global
696 Ionospheric and thermospheric effects of the June 2015 geomagnetic disturbances:
697 multi-instrumental observations and modeling. *J. Geophys. Res.-Space Physics*,
698 V.122, N11, pp. 11,716 - 11,742, doi:10.1002/2017JA024174.
699 Astafyeva, E., I. Zakharenkova, K. Hozumi, P. Alken, P. Coisson, M.R. Hairston, and W.R.
700 Coley. (2018) Study of the Equatorial and Low-latitude Electrodynamic and
701 Ionospheric Disturbances during the 22-23 June 2015 Geomagnetic Storm Using
702 Ground-based and Space-borne Techniques. *J. Geophys. Res. - Space Physics*,
703 V.123, N3, 2424-2440, doi:10.1002/2017JA024981.
704 Bagiya, M. S., K. N. Iyer, H. P. Joshi, S. V. Thampi, T. Tsugawa, S. Ravindran, R.
705 Sridharan, and B. M. Pathan (2011), Low-latitude ionospheric-thermospheric
706 response to storm time electrodynamical coupling between high and low latitudes, *J.*
707 *Geophys. Res.,* 116, A01303, doi:10.1029/2010JA015845.
708 Bagiya M. S., et al. (2014), Effects of prolonged southward interplanetary magnetic field
709 on low-latitude ionospheric electron density, *J. Geophys. Res. Space Physics*, V. 119,
710 5764–5776, doi:10.1002/2014JA020156.
711 Baker, J.B.H. et al. (2007) Observations of ionospheric convection from theWallops
712 SuperDARN radar at middle latitudes*. J. Geophys. Res.*, V. 112, A01303,
713 doi:10.1029/2006JA011982.
714 Balan, N., M. Yamamoto, J. Y. Liu, H. Liu, and H. Lühr (2011), New aspects of
715 thermospheric and ionospheric storms revealed by CHAMP*, J. Geophys. Res.*, 116,
716 A07305, doi:10.1029/2010JA016399.
717 Blagoveshchensky, D. V. and M. A. Sergeeva (2019) Ionospheric parameters in the
718 European sector during the magnetic storm of August 25–26, 2018. *Advances in*
719 *Space Research*, doi:10.1016/j.asr.2019.07.044.
720 Blanc, M., and A. D. Richmond (1980), The ionospheric disturbance dynamo, *J. Geophys.*
721 *Res.*, 85, 1669–1686, doi:10.1029/JA085iA04p01669.
722 Borries, C., J. Berdermann, N. Jakowski, and V. Wilken (2015), Ionospheric storms—A
723 challenge for empirical forecast of the total electron content, *J. Geophys. Res. Space*
724 *Physics*, V. 120, 3175–3186, doi:10.1002/2015JA020988.

725 Christensen, A. B., et al. (2003), Initial observations with the Global Ultraviolet Imager
726 (GUVI) on the NASA TIMED satellite mission, *J. Geophys. Res.*, 108(A12), 1451,
727 doi:10.1029/2003JA009918.
728 Crowley, G., et al. (2006), Global thermosphere-ionosphere response to onset of 20
729 November 2003 storm, *J. Geophys. Res. Space Physics*, 111, A10S18,
730 doi:10.1029/2005JA011518.
731 Crowley, G., D. J. Knipp, K. A. Drake, J. Lei, E. Sutton, and H. Lühr (2010),
732 Thermospheric density enhancements in the dayside cusp region during strong By
733 conditions, *Geophys. Res. Lett.*, 37, L07110, doi:10.1029/2009GL042143.
734 Coxon, J.C., S.E. Milan, J.A. Carter, L.B.N. Clausen, B.J. Anderson, H. Korth (2016)
735 Seasonal and diurnal variations in AMPERE observations of the Birkeland currents
736 compared to modeled results, *J. Geophys. Res. Space Physics*, 121, 4027-4040, doi:
737 10.1029/2015JA021750.
738 Goncharenko, L. P., J. C. Foster, A. J. Coster, C. Huang, N. Aponte, and L. J. Paxton
739 (2007), Observations of a positive storm phase on September 10, 2005, *J. Atmos.*
740 *Sol. Terr. Phys.*, 69, 1253–1272.
741 Förster, M., and S. Haaland (2015), Interhemispheric differences in ionospheric
742 convection: Cluster EDI observations revisited, *J. Geophys. Res. Space Physics*, *120*,
743 doi:10.1002/2014JA020774.
744 Förster, M., S. E. Haaland, and E. Doornbos (2011), Thermospheric vorticity at high
745 geomagnetic latitudes from CHAMP data and its IMF dependence, Ann. Geophys.,
746 29(1), 181–186.
747 Förster, M. and I. Cnossen (2013), Upper atmosphere differences between northern and
748 southern high latitudes: The role of magnetic field asymmetry, *J. Geophys. Res.*
749 *Space Physics*, 118, N9, doi:10.1002/jgra.50554.
750 Fuller-Rowell, T. J., Codrescu, M. V., Moffett, R. J., & Quegan, S. (1994). Response of the
751 thermosphere and ionosphere to geomagnetic storms. *Journal of Geophysical*
752 *Research*, 99(A3), 3893–3914. https://doi.org/10.1029/93JA02015
753 Fuller-Rowell, T. J., Codrescu, M. V., H. Rishbeth, Moffett, R. J., & Quegan, S. (1996) On
754 the seasonal response of the thermosphere and ionosphere to geomagnetic storms,
755 *J. Geophys. Res.,* V.101, 2343-2353, doi:10.1029/95JA01614.
756 Fuller-Rowell, T. J. (2011), Storm-time response of the thermosphere-ionosphere system,
757 in *Aeronomy of the Earth's Atmosphere and Ionosphere, IAGA Spec. Sopron Book*

Ser., vol. 2, edited by M. A. Abdu, D. Pancheva, and A. Bhattacharyya, chap. 32, pp. 419–435, Springer, doi:10.1007/978-94-007-0326-1_32.

Gonzalez, W.D., Joselyn, J.A., Kamide, Y., Kroehl, H.W., Rostoker, G., Tsurutani, B.T., Vasyliunas, V.M. (1994) What is a geomagnetic storm? *J. Geophys. Res.* 99 (A4), 5771–5792.

Greenwald, R. A., Baker, K. B., Dudeney, J. R., Pinnock, M., Jones, T. B., Thomas, E. C., et al. (1995). DARN/SuperDARN: A global view of the dynamics of high-latitude convection. *Space Science Reviews*, 71, 761–796.

Huang, C.-S., Foster, J. C., & Kelley, M. C. (2005). Long-duration penetration of the interplanetary electric field to the low-latitude ionosphere during the main phase of magnetic storms. *Journal of Geophysical Research*, 110, A11309. https://doi.org/10.1029/2005JA011202.

Huba, J. D., Sazykin, S., & Coster, A. (2016). SAMI3-RCM simulation of the 17 March 2015 geomagnetic storm. *Journal of Geophysical Research: Space Physics*, 122, doi:10.1002/2016JA023341, 1246–1257.

Kikuchi, T., & Hashimoto, K. K. (2016). Transmission of the electric fields to the low latitude ionosphere in the magnetosphere-ionosphere current circuit. *Geoscience Letters*, 3(1), 1–11. https://doi.org/10.1186/s40562-016-0035-6.

King, J. H., and N. E. Papitashvili (2005), Solar wind spatial scales in and comparisons of hourly Wind and ACE plasma and magnetic field data, J. Geophys. Res., 110, A02104, doi:10.1029/2004JA010649.

Laundal, K.M., et al. (2017) North-South Asymmetries in Earth Magnetic Field. *Space Science Reviews*, V.206, N1-4, 225-257, DOI: 10.1007/s11214-016-0273-0.

Liu, H., and H. Lühr (2005), Strong disturbance of the upper thermospheric density due to magnetic storms: CHAMP observations, *J. Geophys. Res.*, 110, A09S29, doi:10.1029/2004JA010908.

Liu, H., H. Lühr, V. Henize, and W. Köhler (2005), Global distribution of the thermospheric total mass density derived from CHAMP, *J. Geophys. Res.,* 110, A04301, doi:10.1029/2004JA010741.

Lu et al. (1994) Interhemispheric asymmetry of the high-latitude ionospheric convection pattern. *J. Geophys. Res.*, V. 99, A4, 6491-6510, DOI:10.1029/93JA0344.

Lu, G., L. P. Goncharenko, A. D. Richmond, R. G. Roble, and N. Aponte (2008), A dayside ionospheric positive storm phase driven by neutral winds, *J. Geophys. Res.,* 113, A08304, doi:10.1029/2007JA012895.

March, G., E.D. Doornbos, P.N.A.M. Visser. (2019) High-fidelity geometry models for improving the consistency of CHAMP, GRACE, GOCE and Swarm thermospheric density data sets. *Advances in Space Research*, 63, 213-238, doi: 10.1016/j.asr.2018.07.009.

Mannucci, A. J., G. Crowley, B. T. Tsurutani, O. P. Verkhoglyadova, A. Komjathy, and P. Stephens (2014), Interplanetary magnetic field control of prompt total electron content increases during superstorms, *J. Atmos. Sol. Terr. Phys.*, doi:10.1016/j.jastp.2014.01.001.

Maruyama, N., Richmond, A. D., Fuller-Rowell, T. J., Codrescu, M. V., Sazykin, S., Toffoletto, F. R., et al. (2005). Interaction between direct penetration and disturbance dynamo electric fields in the storm-time equatorial ionosphere. *Geophys. Research Lett.*, 32, L17105. https://doi.org/10.1029/2005GL023763.

Nishitani et al., (2019), Review of the accomplishments of mid-latitude Super Dual Auroral Radar Network (SuperDARN) HF radars, *Progress in Earth and Planetary Science*, 6:27 https://doi.org/10.1186/s40645-019-0270-5.

Paznukhov, V. V., D. Altadill, and B. W. Reinisch (2009), Experimental evidence for the role of the neutral wind in the development of ionospheric storms in mid-latitudes, *J. Geophys. Res.*, 114, A12319, doi:10.1029/2009JA014479.

Pettigrew, E. D., S. G. Shepherd, and J. M. Ruohoniemi (2010), Climatological patterns of high-latitude convection in the Northern and Southern hemispheres: Dipole tilt dependencies and interhemispheric comparisons, *J. Geophys. Res.*, 115, A07305, doi:10.1029/2009JA014956.

Pradipta, R., C. E. Valladares, B. A. Carter, and P. H. Doherty (2016), Interhemispheric propagation and interactions of auroral traveling ionospheric disturbances near the equator, *J. Geophys. Res. Space Physics*, 121, 2462–2474, doi:10.1002/2015JA022043.

Pröss, G. W. (1976) On explaining the negative phase of ionospheric storms, Planet. Space Sci., 24, 607-609.

Prölss, G.W. (1980) Magnetic Storm Associated Perturbations of the Upper Atmosphere: Recent Results Obtained by Satellite-Borne Gas Analyzers. Reviews of Geophysics and Space Physics, V.18, N1, 183-202.

Rideout, W., and A. Coster (2006), Automated GPS processing for global total electron content data*, GPS Solutions*, 10, 219–228, doi:10.1007/s10291-006-0029-5.

825 Ruohoniemi, J. M. and Baker, K. B. (1998) Large-scale imaging of high-latitude convection
826 with Super Dual Auroral Radar Network HF radar observations, *J. Geophys. Res.,*
827 103, 20,797–20,811, doi:10.1029/98JA01288.
828 Swarm Data Handbook, https://earth.esa.int/web/guest/missions/esa-eo-
829 missions/swarm/data-handbook
830 Tsurutani, B., Mannucci, A., Lijima, B., Ali Abdu, M., Sobral, J. H. A., Gonzalez, W., et al.
831 (2004). Global dayside ionospheric uplift and enhancement associated with
832 interplanetary electric fields. *J. Geophys. Res.*, 109, A08302. https://doi.org/10.1029/
833 2003JA010342.
834 Tulunay, Y.K., and J.M. Grebowsky (1987) Hemispheric differences in the morphology of
835 the high latitude ionosphere measured at ~500 km, Planetary and Space Sciences,
836 V35, N6, 821-826, doi:10.1016/0032-0633(87)90043-2
837 Valladares, C. E., & Chau, J. L. (2012). The low-latitude ionosphere sensor network: Initial
838 results. Radio Science, 47, RS0L17. doi :10.1029/2011RS004978.
839 van den IJssel, J., and P. Visser (2007), Performance of GPS-based accelerometry:
840 CHAMP and GRACE. *Advances in Space Research*, 39(10), doi:
841 10.1016/j.asr.2006.12.027
842 van den IJssel, J. A. A. et al. (2014). GPS-based precise orbit determination and
843 accelerometry for low flying satellites, doctoral thesis, TU Delft,
844 doi:10.4233/uuid:9aabcd0f-d984-4d7f-8567-677689e07c85.
845 Vanlommel, P. (2018) Solar-Terrestrial Centre of Excellence (STCE) Newsletter, 20-26
846 Aug 2018, http://www.stce.be/newsletter/pdf/2018/STCEnews20180831.pdf
847 Venkatesh, K., et al. (2019) Super-fountain effect linked with 17 March 2015 geomagnetic
848 storm manifesting distinct F3 layer, *Journal of Geophysical Research*, V. 124, doi:
849 10.1029/2019JA026721.
850 WDC-Kyoto (2018a) http://wdc.kugi.kyoto-u.ac.jp/ae_realtime/201808/index_201808
851 25.html
852 WDC-Kyoto (2018b) http://wdc.kugi.kyoto-u.ac.jp/ae_realtime/201808/index_201808
853 26.html.
854 Wessel, P., & Smith, W. H. F. (1998). New, improved version of the Generic Mapping
855 Tools released. *Eos, Transactions American Geophysical Union*, 79(47), 579.
856 https://doi.org/10.1029/98EO00426

857 Yasyukevich, Yu.V., A.A. Mylnikova, A.S. Polyakova (2015) Estimating the total electron
858 content absolute value from the GPS/GLONASS data, *Results in Physics*, 5, 32-33,
859 doi:10.1016/j.rinp.2014.12.006.
860 Yizengaw, E., Zesta, E., Moldwin, M. B., Damtie, B., Mebrahtu, A., Valladares, C. E., &
861 Pfaff, R. F. (2012). Longitudinal differences of ionospheric vertical density distribution
862 and equatorial electrodynamics. *Journal of Geophysical Research*, 117, A07312.
863 doi:10.1029/2011JA017454
864 Yizengaw, E., Moldwin, M. B., Zesta, E., Biouele, C. M., Damtie, B., Mebrahtu, A., et al.
865 (2014). The longitudinal variability of equatorial electrojet and vertical drift velocity in
866 the African and American sectors. *Annales Geophysicae*, 32(3), 231–238.
867 https://doi.org/10.5194/angeo-32-231-2014.
868 Zakharenkova, I. and E. Astafyeva. (2015) Topside ionospheric irregularities as seen from
869 multi-satellite observations. *J. Geophys. Res. - Space Physics*, V.120, N1, 807-824,
870 doi:10.1002/2014JA020330.
871 Zakharenkova, I., E. Astafyeva and Iu. Cherniak. (2016) GPS and GLONASS
872 observations of traveling ionospheric disturbances during the 2015 St. Patrick's Day
873 storm, *J. Geophys. Res.-Space Physics*, V.121, N12, 12,138-12,156,
874 doi:10.1002/2016JA023332.
875

Figures

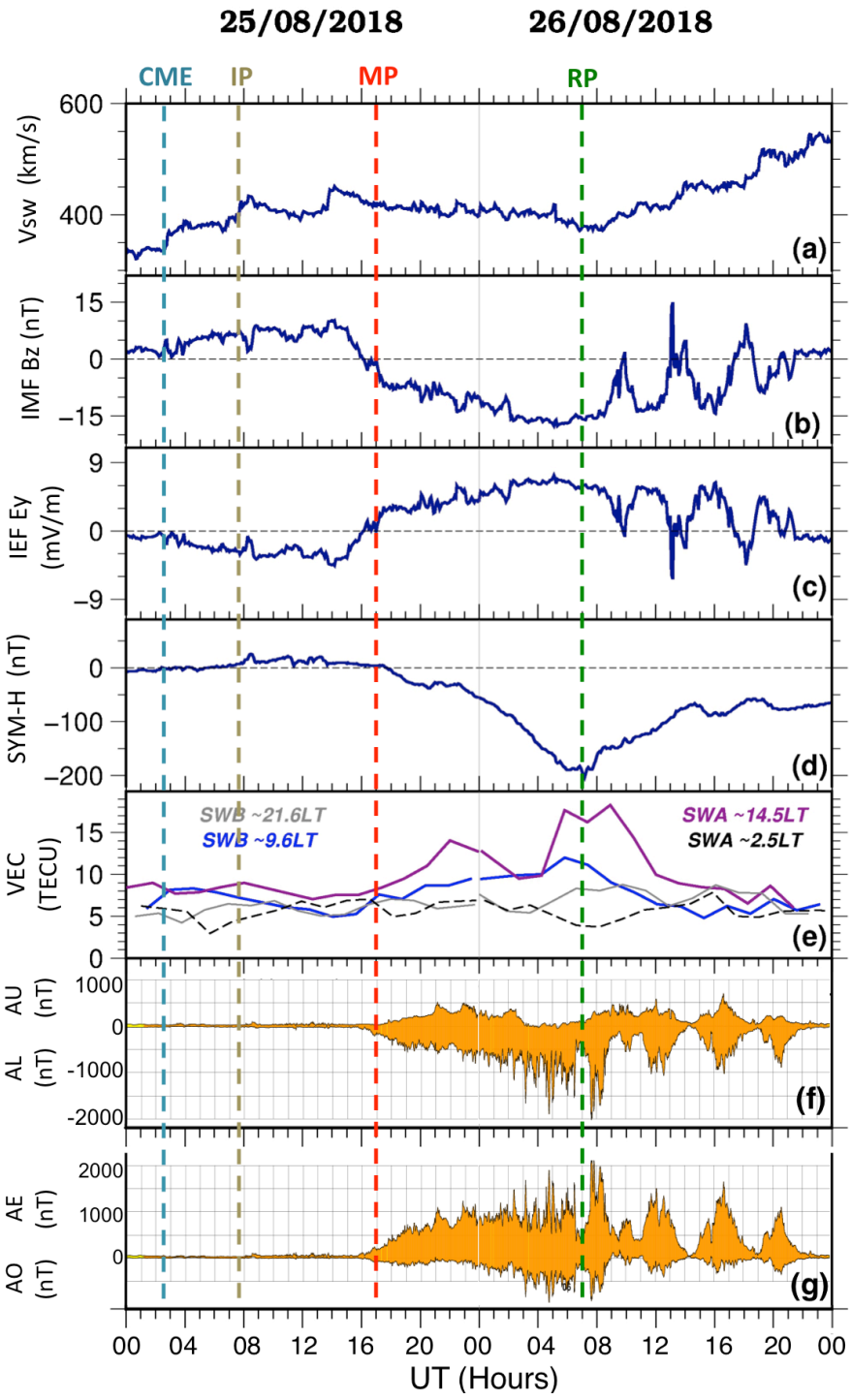

Figure 1. Variations of interplanetary and geophysical parameters on 25-26 August 2018: **(a)** Solar wind speed (Vsw); **(b)** the north-south (Bz) component of the interplanetary magnetic field (IMF) in GSM coordinates; **(c)** the east-west (Ey) component of the Interplanetary Electric field (IEF) estimated as Vsw*IMF Bz; **(d)** SYM-H index; **(e)** vertical electron content (VEC), the topside part of the VTEC calculated from data of GPS-receivers onboard SWA (magenta and black curves) above ~460km and SWB (blue and gray curves) above ~520km; **(f-g)** - AU/AL and AE/AO indices [WDC-Kyoto, 2018a; 2018b]. Label “CME” indicates the time of the CME arrival at 2.75UT. Labels ”IP”, “MP” and “RP” show the beginning of the initial (7.75UT), main (17UT) and recovery (7UT) phases of the storm, respectively.

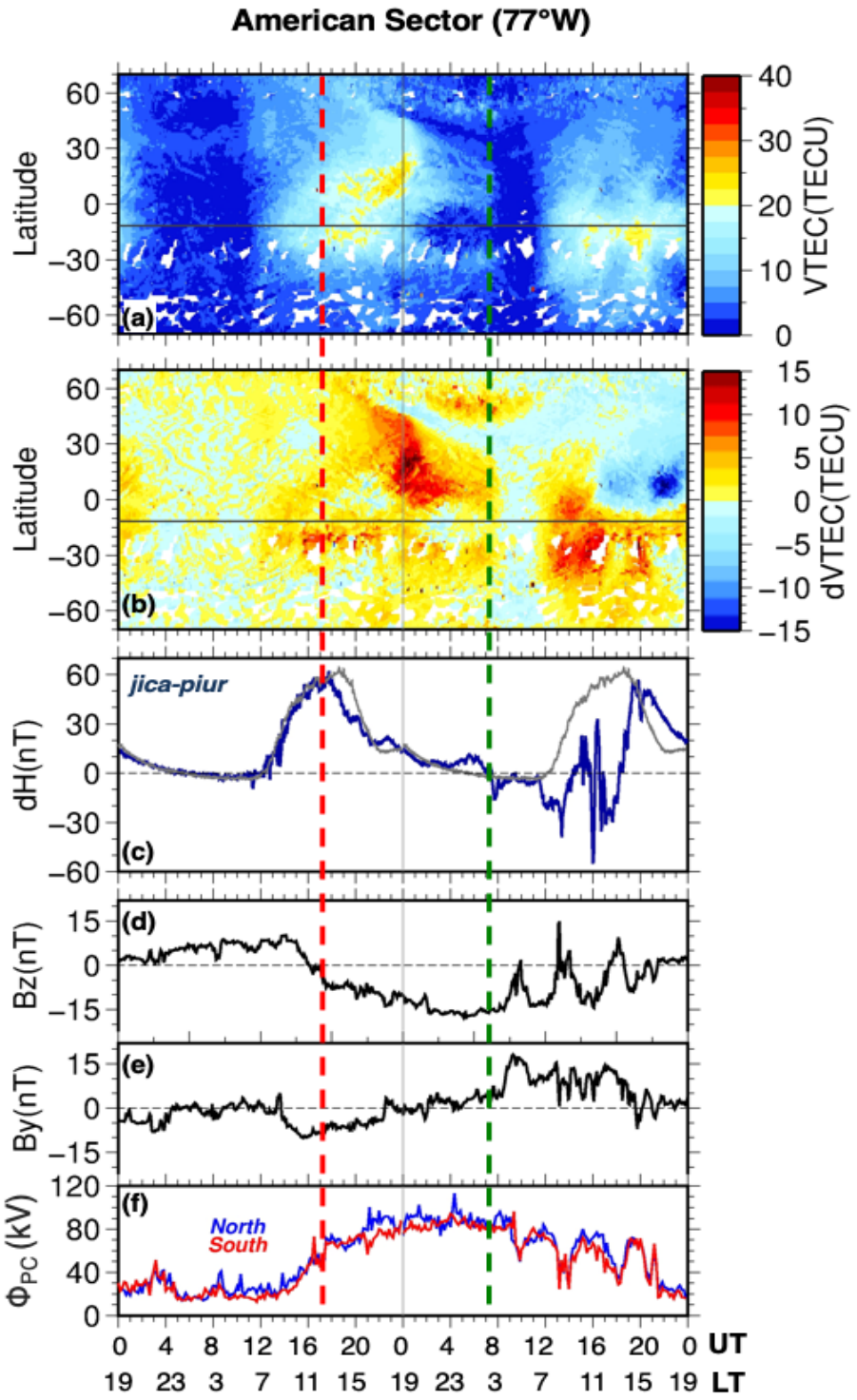

Figure 2. (a, b) Variations of the ionospheric VTEC (a) and the storm-to-quiet residuals dVTEC (b) during the two days of the storm at 77°W. The corresponding color scales are shown on the right. Horizontal gray dotted lines show the position of the magnetic dip equator as of 16 August 2018; **(c)** variations of the horizontal intensity of the geomagnetic field (dH) proportional to the EEJ estimated from a pair of magnetometers *jica-piur*. Gray curve shows the quiet-time reference value; **(d, e)** the IMF Bz (d) and By (e) components in GSM coordinates; **(f)** cross-polar cap potential (Φ_{PC}) on the North (blue) and South (red) poles as derived from SuperDARN. The UT and LT are shown on the bottom. The orange dotted lines show the moment of time when the IMF Bz turned southward and the storm began, and the green dotted line denotes the beginning of the recovery phase.

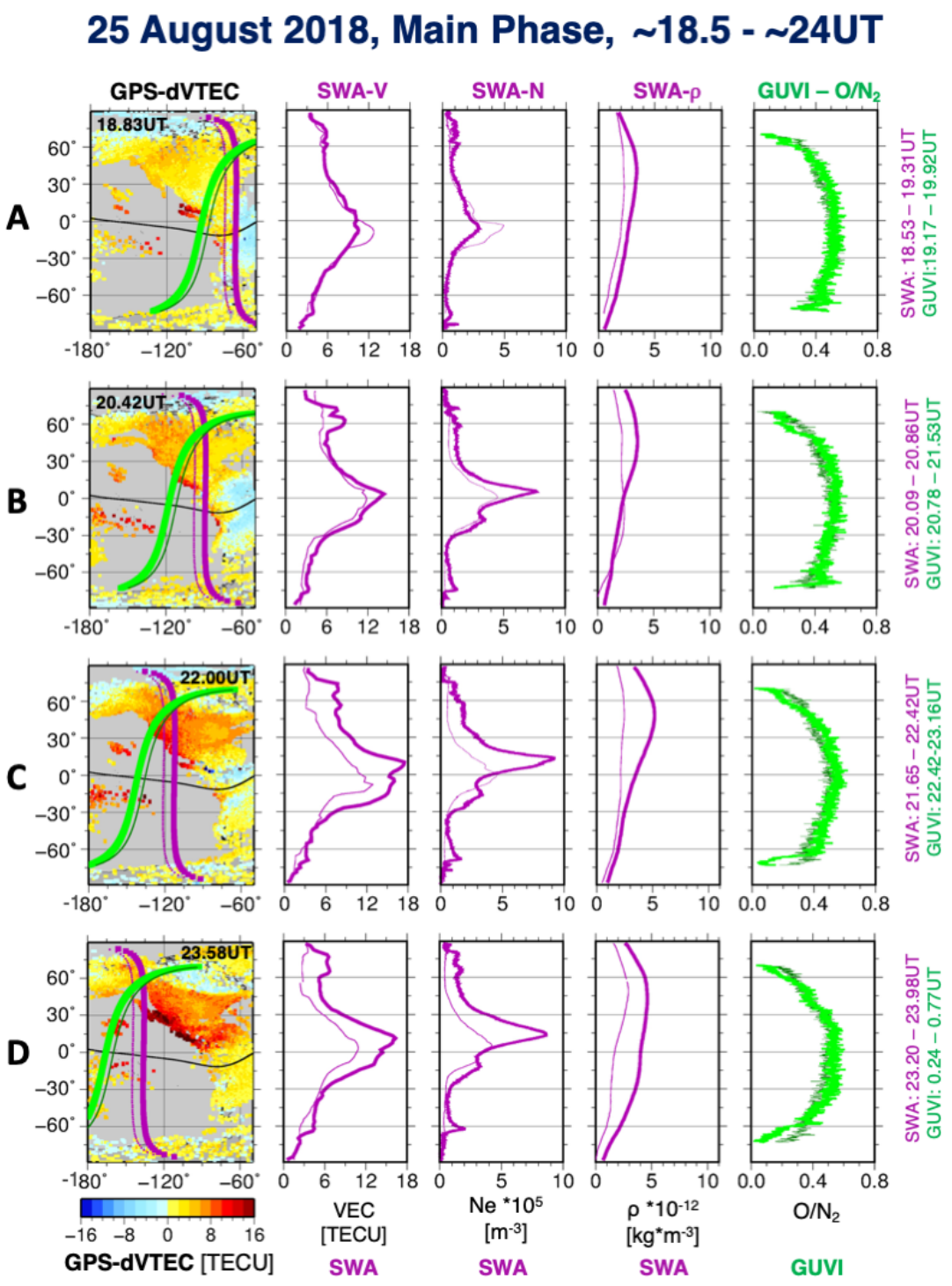

Figure 3. Daytime ionospheric (VEC, Ne) and thermospheric (ρ, O/N2) observations by SWA (thick magenta) and GUVI/TIMED (thick green) during the main phase of the storm (from ~18.5 to ~24UT on 25 August). Thin magenta and thin dark green lines show the quiet-time observations by SWA and GUVI, respectively. The times of the beginning and the end of the satellite half-orbits are indicated on the right marked by the respective colors. The left panels show the positions of the satellite trajectories, and the dVTEC (in colored dots) for the UT of the SWA equatorial crossing. SWA crosses the equator at ~14.4LT, GUVI at ~13.5LT. The dVTEC amplitude scale is shown in the bottom left corner.

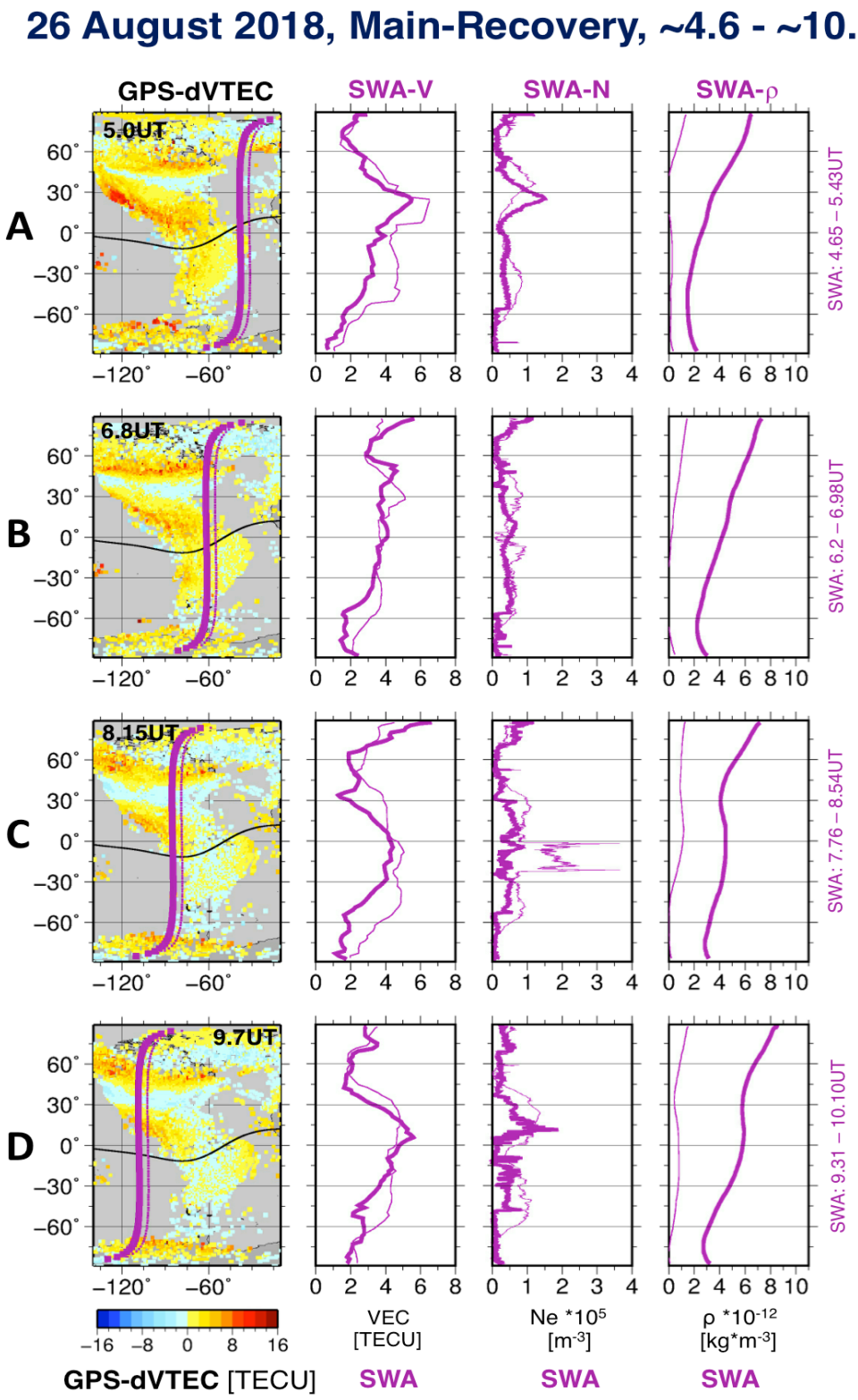

Figure 4. Night-time (~2.4LT) ionospheric and thermospheric observations made by SWA between ~4.6 and ~10UT on 26 August. This period of time corresponds to the end of the main phase and beginning of the recovery phase. Thick and thin curves correspond to storm-time and quiet-time observations. The times of the beginning and the end of the satellite half-orbits are indicated on the right. The left panels show the positions of the satellite trajectories and the storm-to-quiet dVTEC (in colored dots) for the UT when SWA crossed the equator. The dVTEC scale is shown in the left bottom corner. The dVTEC amplitude scale is shown in the bottom left corner.

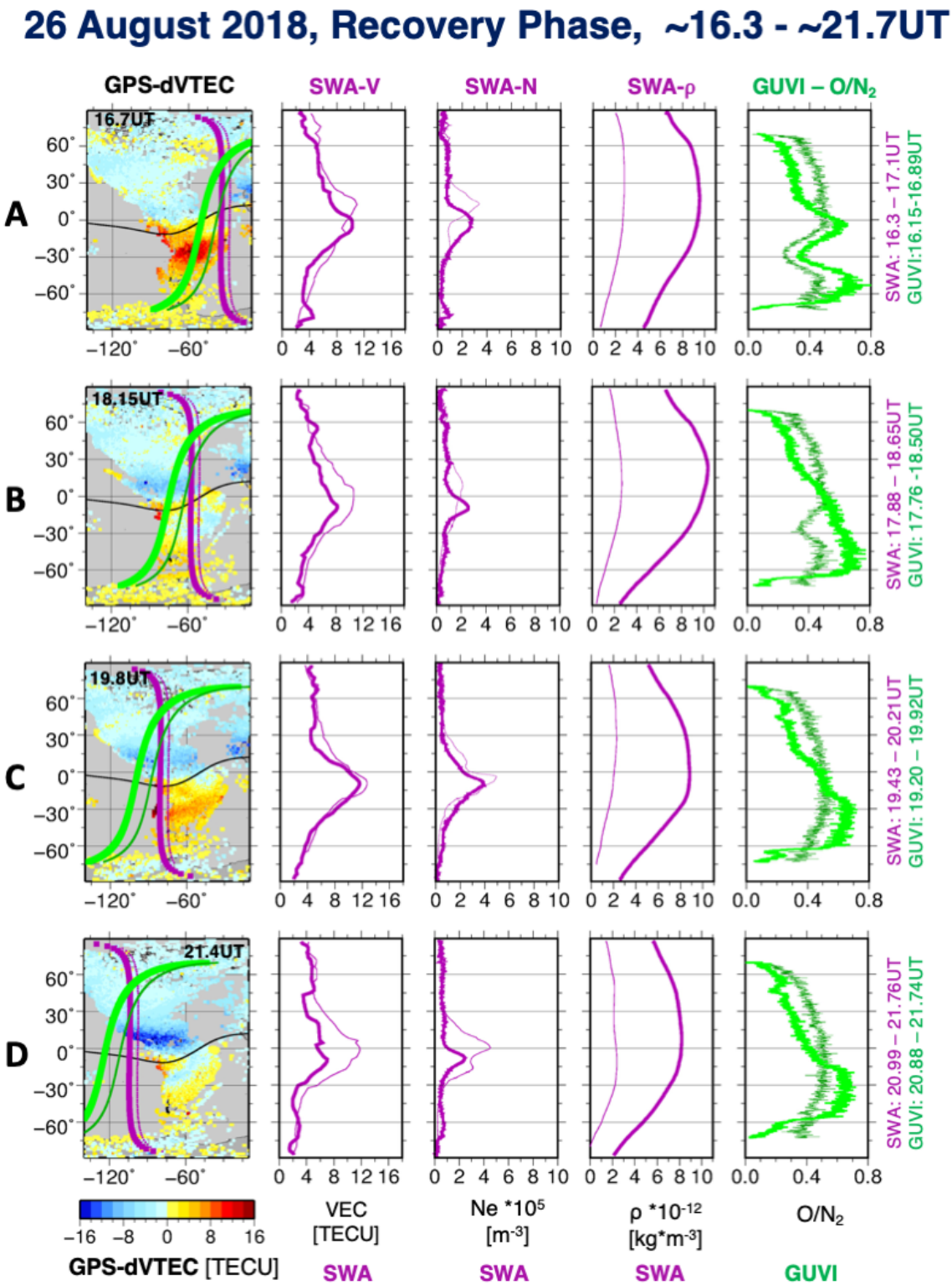

Figure 5. Daytime ionospheric (VEC, Ne) and thermospheric (ρ, O/N2) observations by SWA (thick magenta) and GUVI/TIMED (thick green) during the recovery phase of the storm (from ~16 and ~22UT on 26 August 2018). Thin magenta and dark green lines show the quiet-time observations by SWA and GUVI, respectively. The times of the beginning and the end of the satellite half-orbits are indicated on the right. The left panels show the positions of the satellite trajectories, and the dVTEC (in colored dots) for the UT of the SWA equatorial crossing. SWA crosses the equator at ~14.4LT, GUVI at ~13.5LT. The dVTEC amplitude scale is shown in the bottom left corner.

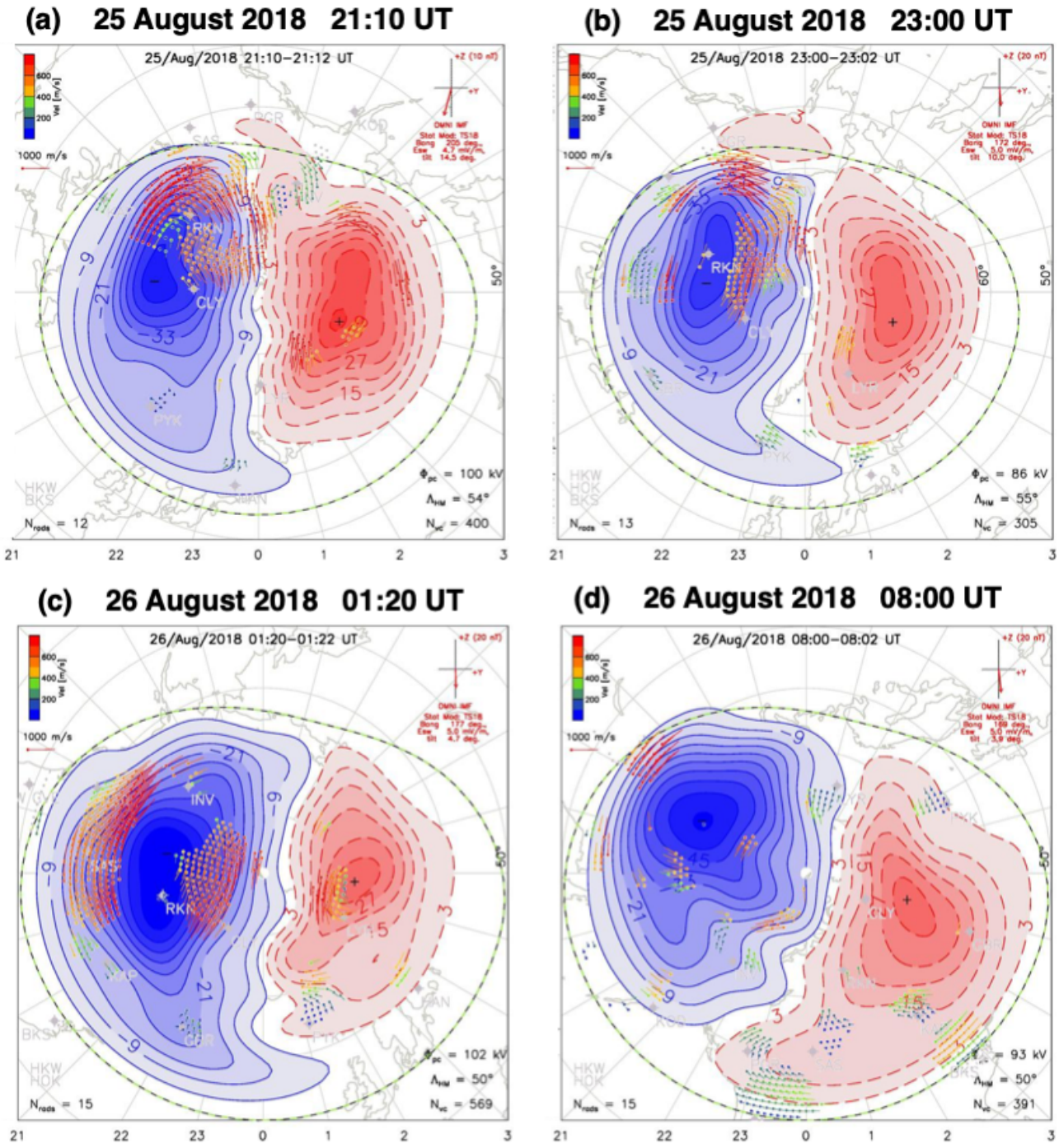

Figure 6. Ionospheric convection patterns determined from SuperDARN radar observations for North polar region for several moments of time on 25-26 August 2018. The date and time are marked on the top of each panel.